

Modelling heat transfer for assessing the convection length in ventilated caves

Amir Sedaghatkish^{1,2}, Claudio Pastore^{1,2}, Frédéric Doumenc^{3,4}, Pierre-Yves Jeannin¹, Marc Luetscher¹

¹ Swiss Institute for Speleology and Karstology (SISKA), CH-2300, La Chaux-de-Fonds, Switzerland

² Center for Hydrogeology and Geothermics (CHYN), University of Neuchâtel, 2000 Neuchâtel, Switzerland

³ Université Paris-Saclay, CNRS, FAST, 91405, Orsay, France

⁴ Sorbonne Université, UFR 919, 4 place Jussieu, F-75252, Paris Cedex 05, France

Corresponding author: Amir Sedaghatkish (amir.sedaghatkish@isska.ch)

Key Points:

- A numerical model was developed to investigate the heat transfer inside ventilated caves driven by chimney effect.
- External thermal perturbations comprise main modes of frequencies including yearly average temperature, yearly and daily fluctuations.
- Air mass flow rate and conduit size are important values for determining the convection length inside the cave.

Abstract

The present study focuses on heat transfer in ventilated caves for which the airflow is driven by the temperature contrast between the cave and the external atmosphere. We use a numerical model that couples the convective heat transfer due to the airflow in a single karst conduit with the conductive heat transfer in the rock mass. Assuming dry air and a simplified geometry, we investigate the propagation of thermal perturbations inside the karst massif. We perform a parametric study to identify general trends regarding the effect of the air flowrate and conduit size on the amplitude and spatial extent of thermal perturbations. Numerical results support the partition of a cave into three regions: (1) a short (few meters) diffusive region, where heat mainly propagates from the external atmosphere by conduction in the rock mass; (2) a convective region where heat is mainly transported by the air flow; (3) a deep karst region characterized by quasi-constant temperatures throughout the year. An estimation of the length of the convective region is proposed and compared to field data from a mine tunnel and two caves. Our results provide first estimates to identify climate sensitive regions for speleothem science and/or ecosystemic studies.

Plain Language Summary

Most ventilated caves are under chimney effect with the airflow driving force controlled by the density difference between inside and outside the cave. Different frequencies can be seen in the external atmosphere temperature but some of them are more significant than others due to their higher amplitude like the yearly average temperature, yearly and daily amplitude of fluctuations. Not only do these thermal fluctuations extend along the cave passages but they also propagate into the surrounding rock within a certain distance. We found this thermal impact depends on the air mass flow rate and conduit size. The convective heat flux is the main cause for the thermal response in ventilated caves. Our results are important for quantitative paleoclimate interpretations of cave records.

1 Introduction

The Understanding heat transfer in karst systems is a key issue for underground biota (Mammola et al., 2019), preservation of cave art (Bourges et al., 2014), speleothem growth rates (Spötl et al., 2005)(Banner et al., 2007), or paleoclimate reconstruction (Borsato et al., 2016)(Casteel and Banner, 2015)(Domínguez-Villar et al., n.d.). However, heat transfer in karst results from an intricate coupling between several mechanisms, including heat conduction in the rock mass (Quindos et al., 1987), convection due to water or air flow in caves (Cropley, 1965), or radiative transfer between cave walls (Guerrier et al., 2019). Latent heat exchanges are also present because of evaporation and condensation on cave walls (Dreybrodt et al., 2005) or ice formation and permafrost (Luetscher et al., 2008). A key issue for the understanding of heat transfer in karst is to determine the processes that dominate in a given configuration, and those that can be neglected.

The simplest heat transfer model of a vadose karst assumes 1D conduction heat transfer in a rock mass of infinite depth with periodic temperature fluctuations at the ground surface. This model predicts that the depth corresponding to 99% attenuation of the temperature fluctuations at the ground surface is a few tens of centimeters for the daily fluctuations and approximately 10 m for

the annual fluctuations. Quindos and co-workers (Villar et al., 1983)(Quindos et al., 1987) measured the monthly mean temperatures in Altamira Cave during a year. They found that the periodic 1D conduction model correctly predicts the amplitude and the phase shift of the annual fluctuations at the cave roof whose depth varied from 3.5 m to 17.5 m. The amplitudes measured at the floors were close to those measured at the corresponding roofs. The phase shifts were slightly larger at the floors but not as large as predicted by the 1D conduction model. The authors attributed this effect to radiative transfer between roofs and floors. Domínguez-Villar et al (2023) and Salmon et al (2023) estimated the thermal diffusivity of the bedrock by fitting the 1D periodic model to temperatures measured at the roof of a weakly ventilated cave. They explained the dispersion of the results by rock heterogeneity.

It has long been known that, in large cave systems, the convective transport of heat by air currents and streams can propagate thermal perturbations over much larger distances than predicted by a pure conduction model. Cropley (1965) found that temperature measurements performed in two caves in West Virginia supported the definition of three zones: zone I immediately adjacent to the cave entrance, where the cave temperature follows the surface temperature fluctuations; zone II where the cave temperature is driven by streams and air currents; zone III where the temperature is approximately constant and close to the annual mean temperature at the surface. Areas where the amplitude of temperature fluctuations was lower than 1°F (*ca.* 0.56°C) around the annual mean temperature were located at more than 1500 m from the cave entrances. This long distance was mainly due to cold water carried into the caves by winter water recharge. Luetscher and Jeannin (2004) defined the heterothermic vadose zone as the surficial part of a karst massif showing seasonal inversions of the temperature gradient, in contrast with the homothermic vadose zone characterized by a temperature gradient close to the lapse rate of humid air (*ca.* 0.5°C 100 m⁻¹). These authors estimated the depth of the heterothermic zone at about 100 m in most cases.

Considerable work has been undertaken to simulate heat transfer by forced convection due to water flow in the vadose and phreatic zones of karst (Gong et al., 2019) (Long and Gilcrease, 2009) (Sinokrot and Stefan, 1993). Covington et al (2011) showed that the relative significance of different heat fluxes including convection and conduction are timescale dependent. Conduction through the rock surrounding a conduit determines heat flux at times of the order of weeks and longer. Coupling convection in water with conduction in rock is thus necessary to get a realistic model valid at all time scales.

The airflow also induces significant convective heat transfer. In closed caves with little or no ventilation, heat transfer between the cave and the external atmosphere is mainly due to conduction in the rock mass. In shallow caves (depth of the order of 10 m), depth variations all along the cave modify the damping and phase shift of the thermal fluctuations, inducing temperature gradients inside the cave, which generate turbulent free convection (Qaddah et al., 2022) and radiative heat transfer (Qaddah et al., 2023). These heat transfer mechanisms contribute in turn to the homogenization of the wall temperature and the deformation of the temperature field in the rock matrix around the cave (Guerrier et al., 2019).

The situation is different when a network of karst conduits has at least two entrances at different elevations. In this configuration, several mechanisms can contribute to the production of airflow through the cave, resulting in significant convective heat transfer between the cave and the external atmosphere. Potential driving forces are barometric fluctuations (Gomell et al., 2021), dynamic pressure effect due to external winds (Kukuljan et al., 2021), diphasic flow due to water

111 circulation (Atkinson, 1977), or the buoyancy due to the density contrast between the inside and
112 the outside of the cave (Gabrovšek, 2023). The latter mechanism is likely the most significant in
113 most cases. The air density depends on moisture content, CO₂ concentration and temperature. In
114 temperate climates, temperature fluctuations are the main cause of density variations
115 (Gabrovšek, 2023). Therefore, the flow direction is upward (resp., downward) when the
116 temperature inside the cave is hotter (resp., colder) than the external atmosphere. In winter, inlets
117 and outlets are thus located at lower and upper entrances, respectively, and the opposite in
118 summer. Due to this seasonal asymmetry, the annual mean temperature is shifted to colder values
119 at lower entrances and warmer values at upper entrances. In alpine ice caves, where this
120 ventilation pattern represents the normal unless the cave is clogged with sediments, these thermal
121 anomalies usually extend over a few hundred meters from the cave entrances (Luetscher et al.,
122 2008).

123 Wigley and Brown (1971) calculated the temperature and moisture content profiles in the air as a
124 function of the distance from the entrance. They used a 1D model based on the energy and water
125 mass conservation in the airflow. The convective heat transfer coefficient between the air and the
126 wall was estimated using an empirical correlation valid for forced convection in smooth pipes.
127 The model assumes prescribed uniform wall temperature, a major simplification that allows to
128 obtain simple closed-form expressions for the temperature and moisture profiles. However, this
129 approach implicitly assumes that the heat flux through the cave wall is convection-limited, and
130 that the rock mass does not play any role. Lismonde (2002) pointed out that the airflow modifies
131 the rock temperature, which in turn changes the air temperature profile in the cave. This author
132 developed a model to predict heat transfer in a straight inclined duct of constant diameter
133 included in a rock massif. The model coupled 1D radial conduction in the rock mass with
134 convective transfer in the gas, using a sinusoidal function of time as inlet temperature. The
135 airflow rate was predicted by considering the interaction between the temperature field in the gas
136 and the airflow through the buoyancy term in the momentum balance equation of the gas. This
137 model reproduced qualitatively some field observations, e.g. the hysteresis of the flow rate or the
138 thermal anomaly in the entrance areas. Gabrovšek (2023) used a similar model to investigate by
139 numerical simulations the effect of conduit shape on the airflow pattern in ventilated caves.

140 The present study focuses on the numerical simulation of heat transfer in ventilated caves for
141 which the airflow is driven by the temperature contrast between the cave and the external
142 atmosphere. We use a numerical model close to that already developed by Lismonde (2002) or
143 Gabrovšek (2023), and we apply it to the simplest possible configuration in order to identify
144 general trends common to most ventilated caves. The convective heat transfer due to dry airflow
145 in a single horizontal karst conduit of constant diameter is coupled with the conductive heat
146 transfer in the impermeable rock mass. We detail in section 2 the governing equations and the
147 related physical assumptions. The method of resolution is briefly outlined in section 3 and
148 detailed in supplemental materials. The parameters used to characterize thermal perturbations are
149 defined in section 4. In section 5, a parametric study investigates the effect of the flowrate and
150 conduit size on the amplitude and spatial extent of the thermal perturbations. A simple
151 expression of the cave length with significant perturbations is proposed. It is compared in section
152 6 with field data from a mine tunnel and two caves. A general discussion is included in section 7.

2 Model definition

2.1 Cave geometry and computational domain

We consider the idealized ventilated cave displayed in Figure 1, located in a rock mass of infinite extent in both vertical directions. The cave consists of a vertical conduit connected by two horizontal conduits to two entrances at different elevations. The rock mass is assumed impermeable. The horizontal conduits are supposed long enough for the vertical conduit to be fully included in the homothermic area where the temperature gradient reduces to the adiabatic lapse rate. The aerologic and thermal problems are uncoupled in this simplified configuration, since the temperature field in the horizontal conduits have no effect on buoyancy. The air flowrate thus only depends on the temperature contrast between the temperature in the vertical conduit, independent of time, and the temperature of the atmosphere outside the cave, a known function of time.

Another source of simplification is that the thermal problems in the regions of upper and lower entrances are uncoupled. They can thus be treated separately. We arbitrarily focus on the upper entrance, but all the results can be easily translated to a lower entrance (the only difference is that the air flows through the upper entrance inward during summer and outward during winter, and vice-versa through the lower entrance).

The computational domain is a cylinder of length L_{dom} and outer radius R_{dom} displayed in red in Figure 1. It contains a conduit of same axis and length and constant radius $R \ll R_{dom}$, inside which the air circulates. The length L_{dom} and outer radius R_{dom} are set so that the computational domain includes the whole thermal perturbation induced in the rock mass by the airflow.

Practically, in a given configuration, L_{dom} and R_{dom} are increased until they no longer influence the results.

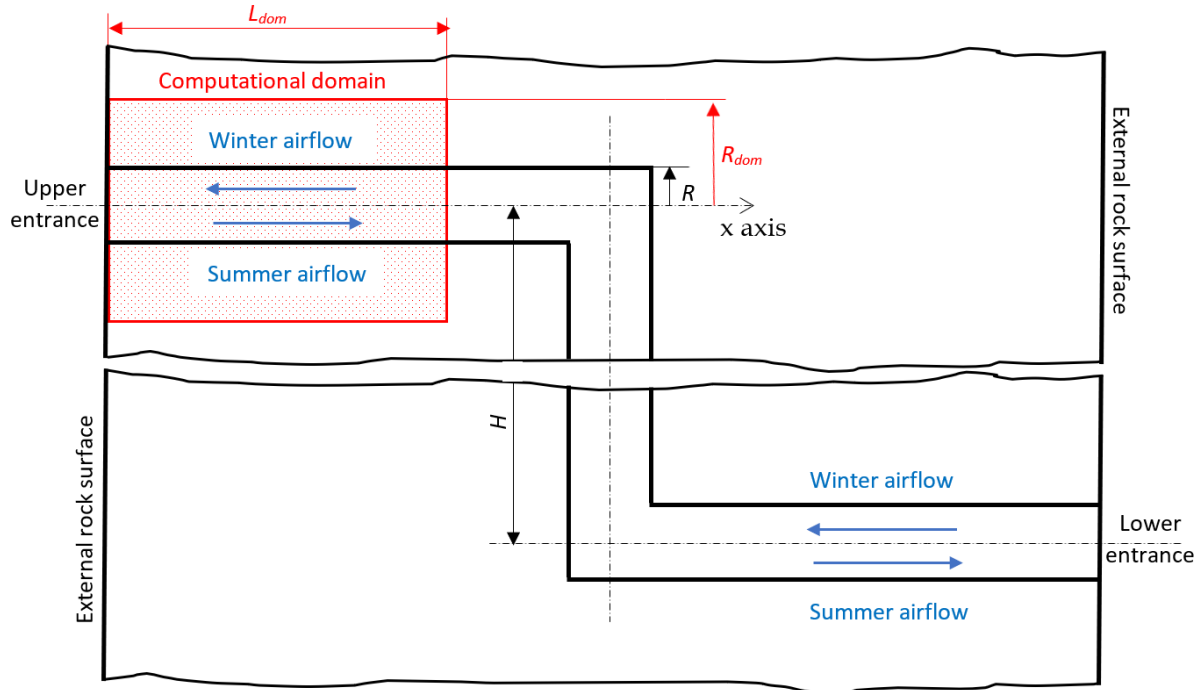


Figure 1: Cave geometry (the computational domain is displayed in red). The rock mass is assumed infinite in both vertical directions.

2.2 Atmosphere temperature and mass flow rate

For the sake of simplification, only the annual fluctuation of the atmosphere temperature T_{atm} are considered. It is thus assumed that $T_{atm}(t)$ follows the simple law:

$$T_{atm}(t) = T_m + \Delta T_y \sin\left(2\pi \frac{t}{\tau_y}\right) \quad (1)$$

where T_m and ΔT_y are the annual mean temperature (AMT) and the amplitude of the annual temperature fluctuation (ATF), respectively, in the external atmosphere at the elevation of the upper entrance. The corresponding period is $\tau_y = 1$ year.

The air mass flow rate \dot{m} is deduced from the momentum balance applied to the air inside the cave. Assuming negligible inertia, the balance between friction and buoyancy yields (Lismonde, 2002):

$$K \dot{m} |\dot{m}| = -(\bar{\rho}_{atm} - \bar{\rho}_m)gH, \quad (2)$$

where H is the length of the vertical conduit and g the gravitational acceleration. The cave aerodynamic resistance K can be assumed constant in the turbulent regime. $\bar{\rho}_{atm}$ and $\bar{\rho}_m$ are the densities of the air outside the cave and inside the homothermic zone, respectively, averaged over the cave height. Assuming that: (1) the difference of densities depends only on the temperature drop between the external atmosphere and the homothermic zone, (2) the temperature field in the vertical conduit follows the AMT in the external atmosphere, we get after linearization:

$$\bar{\rho}_{atm}(t) - \bar{\rho}_m = -\frac{M_a P_{atm}}{R_g T_m^2} (T_{atm}(t) - T_m) \quad (3)$$

where P_{atm} is the atmospheric pressure, M_a the molar mass of air and R_g the ideal gas constant. Eqs. (2) and (3) show that the air flowrate is proportional to the square root of the temperature drop ($T_{atm} - T_m$). Injecting Eqs. (1) and (3) in Eq. (2) yields

$$\dot{m}(t) = S \Delta \dot{m} \sqrt{\left| \sin\left(\frac{2\pi}{\tau_y} t\right) \right|} \quad (4)$$

where $S=-1$ for $T_{atm} < T_m$ (wintertime, upward flow) and $S=+1$ for $T_{atm} > T_m$ (summertime, downward flow). The positive constant $\Delta \dot{m}$ is the amplitude of the annual fluctuation of the flow rate. It is an input of the model.

2.3 Governing equations

The air temperature verifies the energy balance

$$\dot{m} c_{p,a} \frac{\partial T_a}{\partial x} = \varphi_w P \quad (5)$$

where $c_{p,a}$ is the air heat capacity at constant pressure, T_a is the mixing temperature of the air inside the conduit, x the distance from the external rock surface, P the conduit perimeter ($P = 2\pi R$ for a circular cross-section) and φ_w the conductive flux at the conduit wall, positive when going from the rock to the air. Equation (5) is a balance between the energy advected by the air flow (LHS) and the conduction flux at the conduit wall (RHS). The air thermal inertia has

been neglected compared to advection (quasi-steady approximation). Equation (5) requires a single boundary condition at the conduit inlet located at $x=0$ for downward flow ($S=+1$) or at $x=L_{dom}$ for upward flow ($S=-1$). We thus impose the boundary condition

$$T_a(x=0, t) = T_{atm}(t) \text{ for } S=+1 \quad \text{or} \quad T_a(x=L_{dom}, t) = T_m \text{ for } S=-1 \quad (6)$$

The conductive flux φ_w is required to solve Eq. (5). The conduction equation must therefore be solved in the impermeable rock matrix around the cave. The transient 2D axisymmetric conduction equation reads

$$\frac{1}{r} \frac{\partial}{\partial r} \left(r \frac{\partial T_r}{\partial r} \right) + \frac{\partial^2 T_r}{\partial x^2} = \frac{1}{\alpha_r} \frac{\partial T_r}{\partial t} \quad (7)$$

where $T_r(x, r, t)$ is the rock temperature, α_r the rock thermal diffusivity, and r the distance from the cave axis. The boundary conditions are as follows. The atmosphere temperature is imposed on the external rock surface:

$$T_r(x=0, r, t) = T_{atm}(t) \text{ for } R < r < R_{dom} \quad (8)$$

The boundary at $r=R_{dom}$ can be supposed adiabatic because the temperature field only depends on x far from the cave (i.e., for a large value of R_{dom}), and the radial component of the temperature gradient is thus close to zero. The boundary condition at $x=L_{dom}$ is also adiabatic, because this boundary is located in the homothermic zone. We get

$$\frac{\partial T_r}{\partial r}(x, R_{dom}, t) = 0 \text{ for } 0 < x < L_{dom} \text{ and } \frac{\partial T_r}{\partial x}(L_{dom}, r, t) = 0 \text{ for } R < r < R_{dom} \quad (9)$$

The last boundary condition is at the conduit wall. It is given by the Newton's law and the heat flux continuity at the conduit wall:

$$\varphi_w = \lambda_r \frac{\partial T_r}{\partial r}(x, R, t) = h_{th}(t)(T_r(x, R, t) - T_a(x, t)) \quad (10)$$

where λ_r is the rock thermal conductivity, $T_r(x, R, t) = T_w(x, t)$ is the temperature of the conduit wall and h_{th} the heat transfer coefficient. The latter is time-dependent since it depends on the air flowrate $\dot{m}(t)$. All the conditions at the boundaries of the rock domain are displayed in Figure 2. No initial condition is required because we are looking for the periodic regime, i.e., the solution asymptotically reached by the model at infinite time.

2.4 Determination of the heat transfer coefficient

The heat transfer coefficient h_{th} in Eq. (10) is a key parameter. The estimation of h_{th} must therefore be performed with great care to get a reliable model. Assuming forced convection in conduits, Wigley and Brown (1971) and Gabrovšek (2023) used a correlation close to the Colburn correlation (Bergman et al., 2017), valid for fully developed turbulent flow in smooth pipes. Lismonde (2002) pointed out that a cave cannot be considered as a smooth pipe, and multiplied by two the numerical prefactor of the Colburn correlation to account for the effect of wall roughness. Covington et al (2011) used the Gnielinski correlation (Bergman et al., 2017), which explicitly considers the effect of wall roughness.

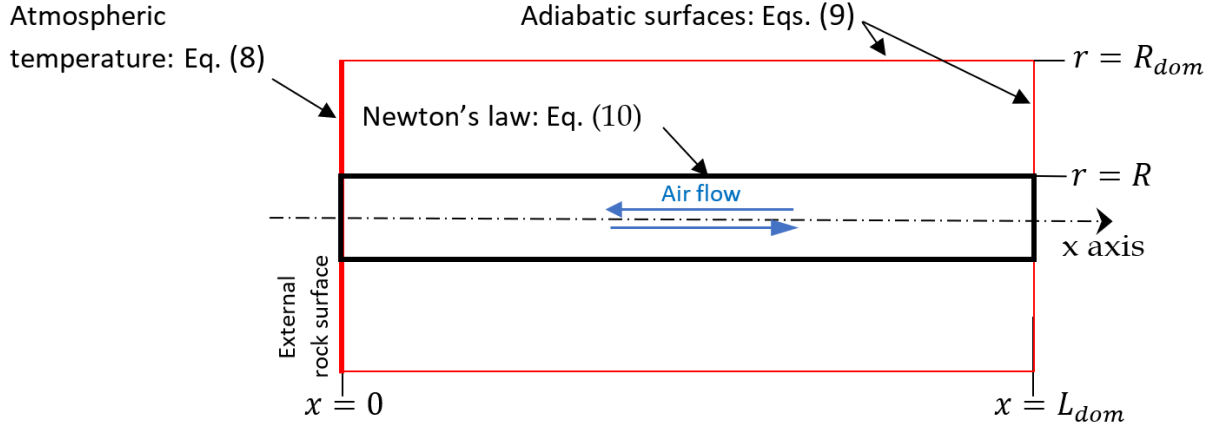


Figure 2: rock domain with the boundary conditions of the heat conduction equation (7).

However, it is unlikely that a cave can be considered as a rough pipe. Indeed, caves can have complicated shapes, ranging from sub-circular conduits with several meters in diameter to complex cave passages associated with the collapse of the host-rock. A succession of bends, conduit contractions or enlargements, or obstacles of any kind are expected to increase the transfer of heat between the air and the wall. Indeed, all of these singularities not only increase the heat exchange surface between the wall and the fluid, but also enhance the heat transfer coefficient by generating secondary flows and by increasing the turbulence level. It is well known that heat exchanger performance can be improved by the insertion of twisted tapes, longitudinal fins or helical ribs inside the tubes (Bergman et al., 2017) (e.g., spirally corrugated tubes can increase the heat transfer coefficient by a factor 3 (Promthaisong et al., 2016)(Pethkool et al., 2011)). However, although empirical correlations exist to predict heat transfer coefficient for a wide range of well-defined geometries used in heat exchangers, no correlation is available for the irregular and tortuous geometries commonly encountered in caves. To get around this difficulty, two distinct cases will be considered. In the first case (case A in the following), correlations for forced convection and fully developed flow in pipes will be used to estimate the heat transfer coefficient. This approach is expected to give a lower bound of the heat transfer coefficient, and thus a lower bound of the heat flux at the conduit wall. In the second case (case B in the following), a higher bound of the wall heat flux will be obtained assuming infinite heat transfer coefficient. Reality must lie between these two limiting cases.

Case A: forced convection and fully developed flow.

The Nusselt number $Nu = \frac{h_{th} D_h}{k_a}$ used for the estimation of h_{th} is displayed in Figure 3 as a function of the Reynolds number $Re_t = \frac{V(t) D_h}{\nu_a}$, for three values of the relative roughness (ε), (k_a and ν_a are the conductivity and the kinematic viscosity of the air, V is the mean air velocity at time t , $D_h = 4A/P$, is the hydraulic diameter with A and P the section and the perimeter of the conduit, the relative roughness ε is the ratio of the roughness over D_h). Nu is computed as follows:

$$Nu = \max(Nu_L, Nu_T) \quad (11)$$

where $Nu_L = 3.66$ is the Nusselt number in the laminar regime (independent of the roughness) and Nu_T is given by the Gnielinski correlation (Bergman et al., 2017):

$$Nu_T = \frac{\left(\frac{f_d}{8}\right) (Re_t - 1000) Pr}{1 + 12.7 \left(\frac{f_d}{8}\right)^{0.5} (Pr^{2/3} - 1)} \quad (12)$$

where Pr is the air Prandtl number ($Pr=0.71$). f_d is the Darcy friction factor which depends on the Reynolds number and the wall relative roughness ε . f_d was estimated using the Haaland correlation (Haaland, 1983):

$$\frac{1}{\sqrt{f_d}} = -1.8 \log \left[\left(\frac{\varepsilon}{3.7} \right)^{1.11} + \frac{6.9}{Re_t} \right] \quad (13)$$

All the simulations were done using $\varepsilon = 0.01$ as a lower bound of the relative roughness in a cave (red curve in Figure 3).

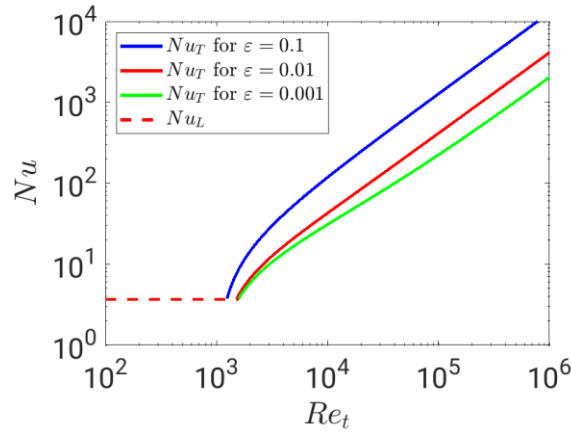


Figure 3: Nusselt number as a function of the Reynolds number (Prandtl number: $Pr=0.71$). The red curve was used for the simulations of case A.

Case B: Infinite heat transfer coefficient

In this case, the conduit wall temperature is equal to the bulk air temperature and Eq.(10) thus reduces to

$$\varphi_w = \lambda_r \frac{\partial T_r}{\partial r}(x, R, t) \quad \text{and} \quad T_r(x, R, t) = T_a(x, t) \quad (14)$$

2.5 Physical properties

All the physical properties are gathered in Table 1. They are assumed constant and estimated at the temperature $T_m = 12^\circ\text{C}$.

Table 1 : Thermophysical properties (estimated at temperature $T_m=285\text{ K} = 12^\circ\text{C}$ and atmospheric pressure $p_{ref} = 101325\text{ Pa}$).

properties	value	Reference
Conduit relative roughness	$\varepsilon = 0.01$	(see section 2.4)
Rock density	$\rho_r = 2320 \frac{\text{kg}}{\text{m}^3}$	(Covington et al., 2011)
Rock heat capacity	$c_{p,r} = 810 \frac{\text{J}}{\text{kg K}}$	(Covington et al., 2011)
Rock thermal conductivity	$k_r = 1.656 \frac{\text{W}}{\text{m.K}}$	(Guerrier et al., 2019)
Rock thermal diffusivity	$\alpha_r = \frac{k_r}{\rho_r c_{p,r}} = 8.81 \times 10^{-7} \frac{\text{m}^2}{\text{s}}$	-
Air dynamic viscosity	$\mu_a = 1.77 \times 10^{-5} \text{ Pa.s}$	(Bergman et al., 2017)
Air density	$\rho_a = 1.23 \frac{\text{kg}}{\text{m}^3}$	(Bergman et al., 2017)
Air kinematic viscosity	$\nu_a = \frac{\mu_a}{\rho_a} = 1.43 \times 10^{-5} \text{ m}^2/\text{s}$	-
Air thermal conductivity	$k_a = 0.0251 \frac{\text{W}}{\text{m.K}}$	(Bergman et al., 2017)
Air Prandtl number	$Pr = \frac{\nu_a}{\alpha_a} = 0.71$	-
Molar mass of air	$M_a = 28.97 \frac{\text{g}}{\text{mol}}$	-
Ideal gas constant	$R_g = 8.314 \frac{\text{J}}{\text{mol K}}$	-

2.6 Dimensionless equations

We define the dimensionless temperatures $\theta_a = (T_a - T_m)/\Delta T_y$ and $\theta_r = (T_r - T_m)/\Delta T_y$ in the air and the rock, respectively. The dimensionless temperature 0 thus corresponds to the external annual mean temperature and 1 is the amplitude of the external annual fluctuations. We take the period $\tau_y = 1$ year as the unit of time and the diffusion length $L_{dif} = \sqrt{\alpha_r \tau_y} \approx 5.3\text{ m}$ as the unit of length. The dimensionless atmospheric temperature θ_{atm} and air flowrate μ are deduced from Eqs.(1) and (4):

$$\theta_{atm}(\tilde{t}) = \sin(2\pi\tilde{t}) \quad (15) \quad \text{and} \quad \mu(\tilde{t}) = \frac{\dot{m}(t)}{\Delta \dot{m}} = S\sqrt{|\sin(2\pi\tilde{t})|} \quad (16)$$

The dimensionless counterparts of Eqs. (5)-(10) read

$$\mu(\tilde{t}) \text{Re} \frac{\partial \theta_a}{\partial \tilde{x}} = \left(4 \frac{k_r}{k_a} \text{Pr}^{-1}\right) \tilde{\varphi}_w, \quad (17)$$

$$\theta_a(\tilde{x} = 0, \tilde{t}) = \sin(2\pi\tilde{t}) \quad \text{for } S=+1 \quad \text{or} \quad \theta_a(\tilde{x} = \tilde{L}_{\text{dom}}, \tilde{t}) = 0 \quad \text{for } S=-1, \quad (18)$$

$$\frac{1}{\tilde{r}} \frac{\partial}{\partial \tilde{r}} \left(\tilde{r} \frac{\partial \theta_r}{\partial \tilde{r}} \right) + \frac{\partial^2 \theta_r}{\partial \tilde{x}^2} = \frac{\partial \theta_r}{\partial \tilde{t}}, \quad (19)$$

$$\theta_r(\tilde{x} = 0, \tilde{r}, \tilde{t}) = \sin(2\pi \tilde{t}) \text{ for } \tilde{R} < \tilde{r} < \tilde{R}_{\text{dom}}, \quad (20)$$

$$\frac{\partial \theta_r}{\partial \tilde{r}}(\tilde{x}, \tilde{R}_{\text{dom}}, \tilde{t}) = 0 \text{ for } 0 < \tilde{x} < \tilde{L}_{\text{dom}} \text{ and } \frac{\partial \theta_r}{\partial \tilde{x}}(\tilde{L}_{\text{dom}}, \tilde{r}, \tilde{t}) = 0 \text{ for } \tilde{R} < \tilde{r} < \tilde{R}_{\text{dom}}, \quad (21)$$

$$\tilde{\varphi}_w = \frac{\partial \theta_r}{\partial \tilde{r}}(\tilde{x}, \tilde{R}, \tilde{t}) = \eta(\tilde{t}) \text{Bi} \left(\theta_r(\tilde{x}, \tilde{R}, \tilde{t}) - \theta_a(\tilde{x}, \tilde{t}) \right), \quad (22)$$

where the tilde (\sim) indicates dimensionless time or lengths. $\eta(\tilde{t}) = \frac{h_{th}(t)}{H_{th}}$ is the heat transfer coefficient scaled by H_{th} , its maximum value reached for $\dot{m} = \Delta \dot{m}$. The Reynolds number $Re = \frac{4 \Delta \dot{m}}{P \mu_a}$ (with μ_a the air dynamic viscosity) and the Biot number $Bi = \frac{H_{th} \sqrt{\alpha_r \tau_y}}{k_r}$ are based on the maximum values $\Delta \dot{m}$ and H_{th} , respectively. $\mu(\tilde{t})Re$ and $\eta(\tilde{t})Bi$ are the Reynolds and Biot numbers at a given time \tilde{t} . In a given configuration, \tilde{R}_{dom} and \tilde{L}_{dom} that define the size of the computational domain are increased until they do not modify the results, as stated in section 2.1. With the constant physical properties defined in Table 1, a configuration is well-defined if only two dimensionless numbers are known: the dimensionless conduit radius \tilde{R} and the Reynolds number Re . In case A, i.e., when fully developed forced convection is assumed for the estimation of the heat transfer coefficient, the Biot number in Eq. (22) is related to the Nusselt number by the simple relation $\eta(\tilde{t})Bi = \frac{Nu}{\tilde{R}} \left(\frac{k_a}{2k_r} \right)$, where Nu depends on $Re_{\tilde{t}} = \mu(\tilde{t})Re$ through Eqs.(11)-(12). In case B, the Biot number is infinite, i.e., $\eta(\tilde{t})Bi \rightarrow \infty$. Eq. (22) thus reduces to

$$\tilde{\varphi}_w = \frac{\partial \theta_r}{\partial \tilde{r}}(\tilde{x}, \tilde{R}, \tilde{t}) \quad \text{and} \quad \theta_r(\tilde{x}, \tilde{R}, \tilde{t}) = \theta_a(\tilde{x}, \tilde{t}) \quad (23)$$

3 Method of resolution

We are looking for the periodic solution of the mathematical model defined in section 2.6. The periodic regime could be obtained by time integration starting from an arbitrary initial condition, after simulating a number of cycles large enough to get a good approximation of the solution at infinite time. However, the slow convergence of this method can generate large computational times. We thus prefer to use another method, based on Fourier series. All time-varying variables, including the temperatures in the rock and in the air, are approximated by truncated Fourier series and inserted in the mathematical model of section 2.6. This yields a set of coupled partial differential equations (PDE), which does not include the time. The numerical resolution by the Galerkin method of this set of PDE gives the spatial distribution of the amplitude and phase of the Fourier modes. The temporal evolution of the dependent variables is then recovered from Fourier series. This method is detailed in supplemental material. The validation by comparison with a standard time integration method is presented in the same appendix. All the numerical simulations were performed with the commercial software Comsol Multiphysics, version 6.1.

4 Characterization of the thermal perturbation

Figure 4 displays the wall and air temperatures inside the cave at different distances from the entrance, for case A with $\tilde{R} = 0.189$ and $Re = 1.8 \times 10^5$. Figure 4-left shows the amplitude of the Fourier modes that stems directly from the numerical simulation. The mode k refers to the dimensionless period $1/k$. The amplitudes of the modes $k=0$ and $k=1$ are thus the annual mean

temperature (AMT) and the amplitude of the annual temperature fluctuation (ATF), respectively. The modes $k=2$, $k=3$, and so on, refer to the periods 6 months, 4 months, etc. Although the external temperature imposed at $\tilde{x} = 0$ contains the single mode $k=1$ (since it reduces to the simple sine function of Eq. $\theta_{\text{atm}}(\tilde{t}) = \sin(2\pi\tilde{t})$ (15)), the coupling between modes due to convection results in the existence of other modes than $k=1$ in cave temperatures (modes $k=0$ to 18 were considered in the simulations, see supplemental material). Figure 4-right displays the periodic time series built from the Fourier series. The amplitude of the temperature fluctuations decreases when the distance from the entrance increases, as expected. The hot thermal anomaly expected at the vicinity of an upper entrance is also observed. Indeed, for $\tilde{x} = 10$ to 10^3 , the dimensionless temperature is positive throughout the year, which means that it is always higher than the external AMT, even in winter.

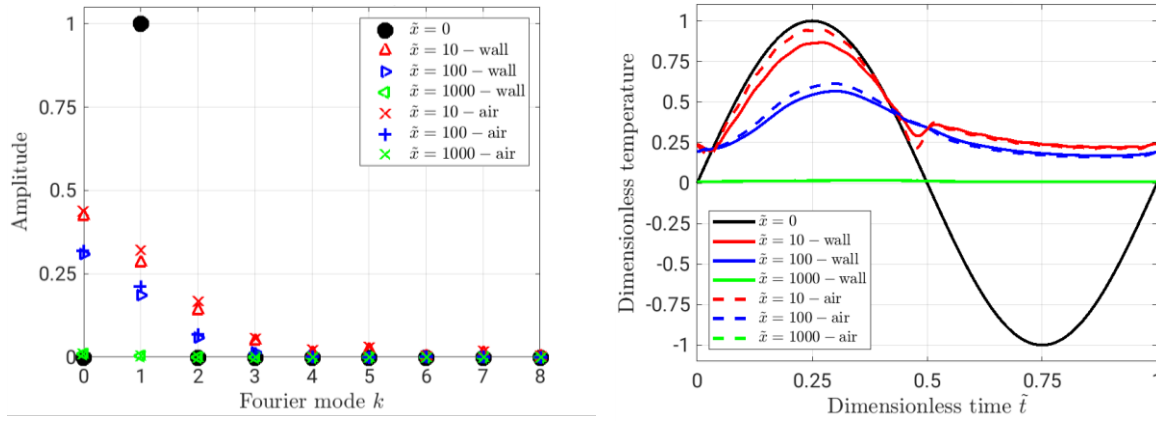


Figure 4. Wall and air temperatures at different distances \tilde{x} from the entrance. Left: amplitude of the Fourier modes, right: time series. Case A with $\tilde{R}=0.189$ and $\text{Re}=1.8 \times 10^5$.

Figure 5-left displays the temperature profiles in the air and at the cave wall, at different times of the year. Following an approach similar to that of Cropley (1965), we split the cave into three zones.

- 1- A first zone, from $\tilde{x} = 0$ to $\tilde{x} \approx 1$ (the diffusion length), where the cave temperature follows the fluctuations of the external temperature. More precisely, the sign of the temperature gradient changes in summer and winter (see the inset in Fig.5-left). This first zone is dominated by the temperature fluctuations of the external wall, propagating inside the rock mass by heat conduction. It will be called diffusive region in the following.
- 2- A second zone characterized by a positive dimensionless temperature and reduced but significant fluctuations. In the specific case of Figure 5-left, it approximately extends from $\tilde{x} \approx 1$ to 10^3 . In this zone, heat diffusion from the external wall is negligible compared to convection. It will be called convective region in the following. Because of the seasonal flow reversals, the inlet temperature of the air flow is 1 in summer (inward flow) and 0 in winter (outward flow, coming from the deep karst). As a consequence, this zone does not “feel” the negative winter temperatures. This results in: (1) a shift of the AMT to positive values, the so-called thermal anomaly, (2) a reduction of the amplitude of the fluctuations, because the temperature oscillates between 0 and 1 whereas the external temperature fluctuates between -1 and 1.

- 3- A third zone, called deep karst in the following, where the dimensionless temperature is approximately constant and close to zero (the external AMT).

These three regions appear clearly on the amplitude of the Fourier modes plotted in Figure 5-right as a function of the distance from the entrance \tilde{x} . The amplitude of the mode $k=1$ (i.e. the ATF) decreases in two steps. It first drops down from 1 to 0.3 in the diffusive region (from $\tilde{x} = 0$ to $\tilde{x} \approx 1$), then slowly decreases in the convective region, over a distance much longer than 1 (of the order of 10^3 in the specific case of Figure 5). The amplitude of the mode $k=0$ (i.e. the AMT) increases in the diffusive region, then reaches a quasi-plateau and slowly decreases in the convective region, over a distance of the same order as for the mode $k=1$. The modes such that $k \geq 2$ follow qualitatively the behavior of mode $k=0$, with a lower amplitude and a shorter attenuation length. In the following, we will focus on both modes with the highest amplitude, $k=0$ and $k=1$, as representative of the AMT (the thermal anomaly) and the ATF, respectively.

In all the simulations we did, the transition between the diffusive and convective regions always take place at a distance from the entrance of the order of 1, as expected. Conversely, the characteristics of the convective domain (amplitude of the thermal perturbation and its spatial extent) depend on the model parameters: the Reynolds number Re (containing the air flow rate) and the cave radius \tilde{R} . This dependence will be systematically investigated in the parametric study of the next section. In order to facilitate the interpretation of the results, we define a small number of relevant parameters characterizing the perturbation of the cave temperature field by the air flow. The magnitude of the perturbation is characterized by the AMT and the ATF at the beginning of the convective region, where the impact of convection is maximum, and the effect of thermal conduction from the external wall negligible. We define $\Delta\theta_w$ as the maximum amplitude of the mode $k=1$ in the convective region, for the wall temperature. Practically, it is evaluated at the change of slope noticed on the solid blue line in the inset of Figure 5-right. Similarly, $\bar{\theta}_w$ is the maximum amplitude reached by the mode $k=0$ for the wall temperature (maximum of the red solid line in the inset of Figure 5-right). The corresponding amplitudes for the air temperature, $\Delta\theta_a$ and $\bar{\theta}_a$, are estimated at the same location as $\Delta\theta_w$ and $\bar{\theta}_w$, respectively. For example, in the specific case of Figure 5, we get $\Delta\theta_w \approx 0.30$ and $\Delta\theta_a \approx 0.34$ (maximum ATF), $\bar{\theta}_w \approx 0.42$ and $\bar{\theta}_a \approx 0.44$ (maximum AMT).

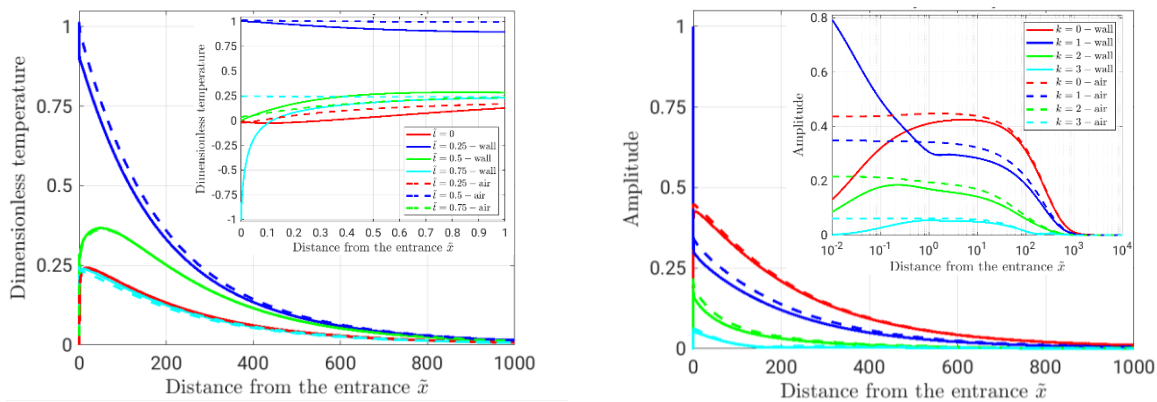


Figure 5. Wall (solid lines) and air (dashed lines) temperatures as a function of the distance \tilde{x} from the entrance. Left: temperature profiles at various times (Inset: zoom in the diffusive region), right: amplitude of the Fourier modes $k=0$ to 3 (Inset: log scale on the \tilde{x} -axis). Case A with $\tilde{R}=0.189$ and $Re=1.8 \times 10^5$.

The four parameters $\bar{\theta}_w$, $\bar{\theta}_a$, $\Delta\theta_w$ and $\Delta\theta_a$ represent the maximum amplitudes of the perturbation in the convective region. These amplitudes decrease with the distance from the entrance, as the heat transported by the air flow is gradually dissipated by conduction in the rock mass. We arbitrarily assume that a Fourier mode has been damped when its amplitude has been divided by 10. Figure 6-left shows the thermal perturbation in a rock massif with the black solid lines corresponding to an AMT equal to $\bar{\theta}_w/10 = 0.042$. The rock domain thus defined can be characterized by the length \tilde{L}_0 along the cave axis and the maximum width \tilde{W}_0 along the radial direction. Similarly, the black solid lines in Figure 6-right correspond to an ATF equal to $\Delta\theta_w/10 = 0.030$. The size of the corresponding domain is characterized by its length \tilde{L}_1 and its width \tilde{W}_1 . The latter is taken close to the entrance, but out of the diffusive region. The lengths \tilde{L}_0 and \tilde{L}_1 can also be estimated from the air temperature (length such that the amplitude of AMT and ATF in the air are equal to $\bar{\theta}_a/10$ and $\Delta\theta_a/10$, respectively).

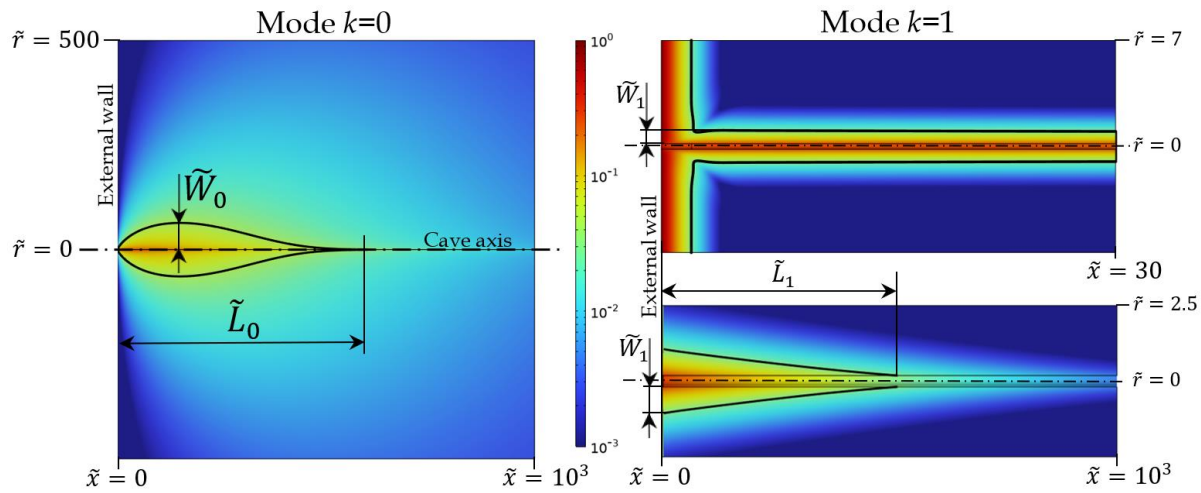


Figure 6. Amplitude contour of the thermal perturbation in a symmetry plane of the rock massif. Left: mode $k=0$; the black solid lines correspond to the amplitude $\bar{\theta}_w/10 = 0.042$ (n.b.: at the scale of the figure, the cave reduces to a line). Right: mode $k=1$; the black solid lines correspond to the amplitude $\Delta\bar{\theta}_w/10 = 0.030$ (n.b.: the top view focuses on the entrance region; the bottom view has been plotted with different scales on \tilde{x} and \tilde{r} to display the whole perturbed region). Case A with $\tilde{R}=0.189$ and $Re=1.8\times 10^5$.

5 Parametric study

We first analyze in section 5.1 the effect of the airflow on the maximum thermal perturbation, at the beginning of the convective region. We then investigate in section 5.2 how the thermal perturbation decreases with the distance from the entrance.

5.1 Amplitude of the thermal perturbation induced by the air flow

Figure 7 displays the AMT ($\bar{\theta}_w$ and $\bar{\theta}_a$) and the ATF ($\Delta\theta_w$ and $\Delta\theta_a$) at the beginning of the convective region. Cases A and B yield close values of $\bar{\theta}_a$, which is also little sensitive to the model parameters Re and \tilde{R} . Indeed, $\bar{\theta}_a$ varies only from 0.25 to 0.6 when Re and \tilde{R} are increased

by three and two orders of magnitude, respectively. With the exception of small conduits ($\tilde{R} = 0.2$) at small Reynolds number ($Re \lesssim 3 \times 10^3$), a similar remark can be made on $\Delta\theta_a$.

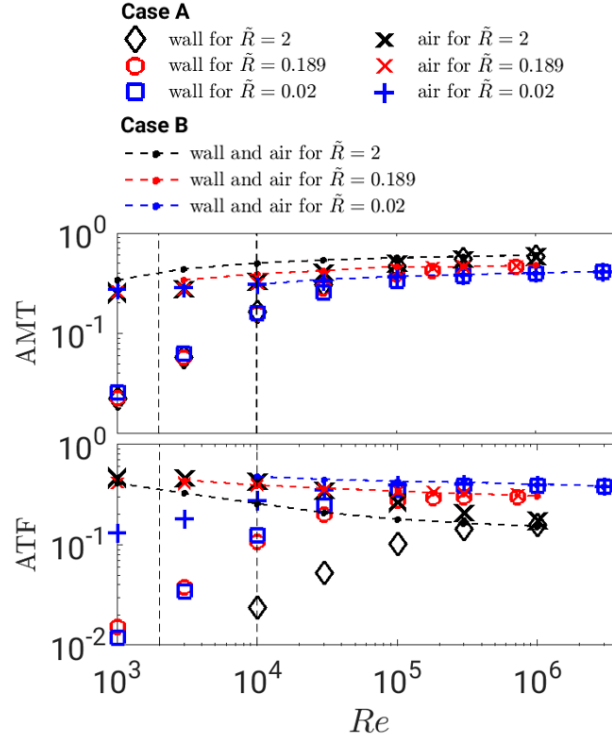


Figure 7: maximum thermal perturbation at the beginning of the convective region for cases A (Biot number estimated from forced convection correlations) and B (infinite Biot number). Top: maximum AMT ($\bar{\theta}_w$ and $\bar{\theta}_a$ for the wall and the air, resp.). Bottom: maximum ATF ($\Delta\theta_w$ and $\Delta\theta_a$ for the wall and the air, resp.). The vertical dashed lines correspond to the limits of the laminar and turbulent regimes.

The evolution of the wall temperature is more intricate. In case B, the assumption of infinite Biot number imposes $\bar{\theta}_w = \bar{\theta}_a$ and $\Delta\theta_w = \Delta\theta_a$ (since the air and wall temperatures are equal). Assuming that Case A provides a lower bound of the actual Biot number in a cave, Eq.(14) allows to estimate the consequences of an error in the determination of the Biot number on the estimation of the wall temperature at the beginning of the convective region. At high Reynolds number ($Re \gtrsim 3 \times 10^5$), no accurate estimation of the relation of the function $Nu(Re)$ is required because the heat transfer is completely driven by heat conduction in the rock massif. Conversely, the relation $Nu(Re)$ is a key information for convection-limited heat transfer at small Reynolds number ($Re \lesssim 10^4$). At intermediate Re , an accurate estimation of Nu is required to get the ATF of the wall in a cave with a large radius ($\tilde{R} \gtrsim 1$).

5.2 Spatial extent of the thermal perturbation induced by the air flow

The characteristic lengths \tilde{L}_0 and \tilde{L}_1 for the damping of the AMT and ATF along the cave axis are displayed in Figure 8. The values of \tilde{L}_0 computed in case B (infinite Biot number) support the simple relation obtained from curve fitting:

$$\tilde{L}_0 \approx 3.1 \times 10^{-3} Re^{1.06} \tilde{R}^{0.61} \quad (24)$$

In case A, estimating \tilde{L}_0 from the air or the wall temperatures give the same results (the lengths required to get $\bar{\theta}_a$ or $\bar{\theta}_w$ divided by 10 are the same, even when $\bar{\theta}_a$ and $\bar{\theta}_w$ are different). At high Reynolds number, \tilde{L}_0 estimated from case A follows Eq.(24) derived for case B, as expected when heat transfer is conduction-limited. When Re is decreased, using the forced convection correlations of case A reduces the heat flux at the cave wall compared to the infinite Biot number of case B, leading to larger values of \tilde{L}_0 than predicted by Eq. (24).

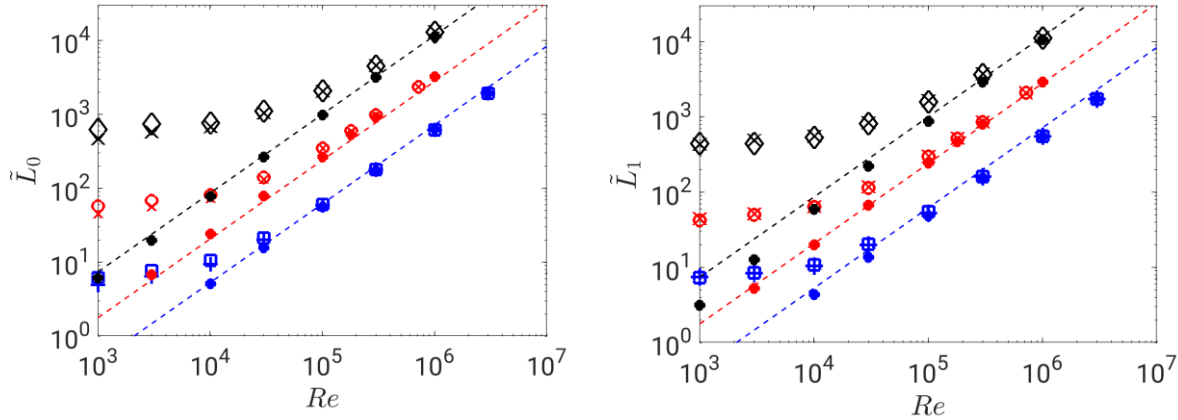


Figure 8: characteristic lengths \tilde{L}_0 (left) and \tilde{L}_1 (right) as a function of the Reynolds number Re for various radius \tilde{R} , computed from wall or gas temperatures. The dashed lines correspond to Eq.(24). Symbols: same legend as in Figure 7.

\tilde{L}_1 , the distance corresponding to the damping of the ATF, is nearly equal to \tilde{L}_0 , with the exception of slight differences at low Reynolds number for $\tilde{R}=2$ (see Figure 8-right). The length of the convective region (called convection length in the following) can thus be indifferently determined from the damping of the AMT or ATF, based on the wall or the air temperatures. A higher bound of the convection length is provided by case A, while case B provides a lower bound. We can see in Figure 8 that the uncertainty on the convection length increases when the Reynolds number Re is decreased and when the cave diameter \tilde{R} is increased.

The width \tilde{W}_0 corresponding to the damping of the AMT in radial directions inside the rock mass is displayed in Figure 9. It is approximately proportional to \tilde{L}_0 and an order of magnitude smaller.

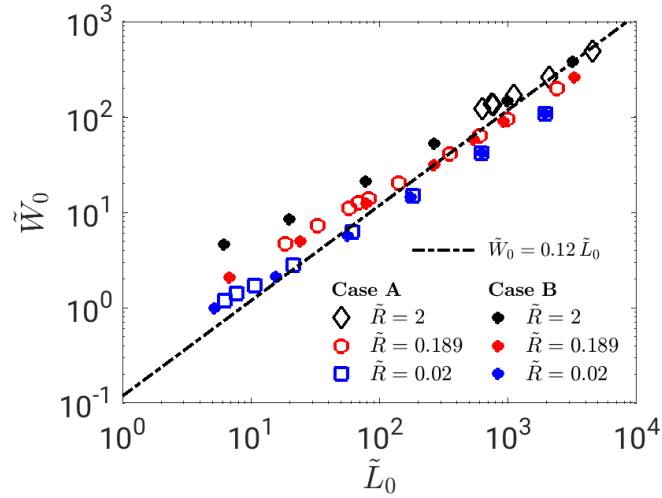


Figure 9: width \tilde{W}_0 corresponding to the damping of the AMT in the radial directions inside the rock mass

6 Comparison with field data

This section tests our model against the field data obtained from a mine and two caves with significant ventilation. More specifically, this comparison is aimed at establishing whether the model developed in section 2 is relevant to predict the right order of magnitude of the convection length.

6.1 Baulmes mine (Switzerland)

The Baulmes mine (46°47'33"N, 6°31'35"E, 655 m a.s.l.) is located in western Switzerland. This mine comprises a network of 11 sub horizontal levels with a cumulated length of about 17 km (Figure 10). The difference in elevation between the uppermost and lowest entrances is 90 m, ensuring a strong chimney effect. In the vertical section of this mine, most of the conduits are dead end as can be seen in Figure 10 (more information about Baulmes mines is found in ref (Bourret et al., 2007)). The temperature delivered by Mathod weather station (46°44'13"N, 6°34'4"E, 435 m a.s.l., at 7 km SW from the study site) is used as an estimation of the external atmosphere temperature. A correction has been applied to account for the difference of elevation with the mine entrance, using the vertical thermal gradient -5.2°C/km (mean value from the network of swiss meteorological stations for the time range 1991-2020). The resulting external temperature is displayed in Figure 11 for one year from July 1st 2022 at 0h00 (this date is taken as time $t = 0$ for all the data from Baulmes mine). The sampling period was 1 hour. The FFT of the external atmosphere temperature yielded $T_m = 10.4^\circ\text{C}$ (after correction) and $\Delta T_y = 9.4^\circ\text{C}$ for the external AMT and ATF, respectively.

The 360 m long tunnel #10 is connected horizontally to the lower entrance with no connection to other branches. This is the zone of interest of study. It is indicated by the yellow shading in Figure 10. This conduit has a typical horseshoe cross section. The geometrical characteristics of this conduit, including the mean perimeter and cross section area, their standard deviation as well as its total length are summarized in Table 2. We instrumented this tunnel with seven temperature probes at different distances from the entrance. They are listed in Table 3. The first

485 six temperature probes are Reefnet (Sensus Ultra) with ± 0.3 °C accuracy. The last one located at
 486 360 m from entrance is HOBO (u22-001) with ± 0.2 °C accuracy. The temperature inside the
 487 conduit was recorded by these seven probes from February 3rd 2023 ($t = 0.596$ year) to July 7th
 488 2023 ($t = 1.017$ year). This time range is displayed by the horizontal arrow in Figure 11. The
 489 sampling period was 1 hour.

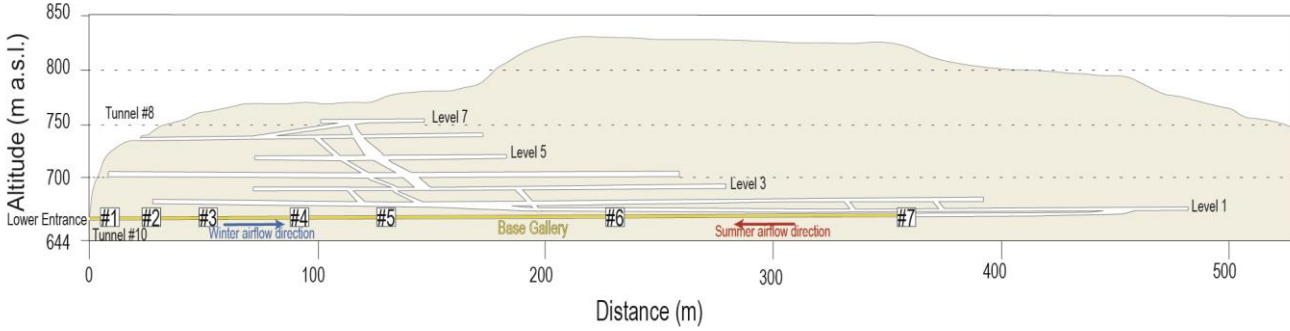


Figure 10: map of Baulmes mine (vertical)

490
 491
 492 Table 2: Geometrical characteristics of the instrumented conduit of Baulmes mine (length L_c , mean value and
 493 standard deviation of the perimeter P and the cross-section A).

L_c (m)	P (m)		A (m ²)	
	Mean (n= 28)	std	Mean (n= 28)	std
360	9.7	1.1	6.6	1.5

494
 495 Table 3: location of the seven temperature probes inside the instrumented conduit of Baulmes mine. x is the distance
 496 from the lower entrance.

Probe	#1	#2	#3	#4	#5	#6	#7
x (m)	10	26	50	90	128	220	360
$\tilde{x} = x/L_{dif}$	1.9	4.9	9.4	17	24	42	68

497
 498 The air mass flow rate was measured sporadically with a manual hot wire anemometer (Testo425
 499 with an accuracy of $0.03 \text{ m/s} \pm 5\%$ of the measured value). The measurements were carried out at
 500 the four dates listed in Table 4 and displayed by vertical red bars in Figure 11. There are two
 501 dates in winter and two in summer. The mean flowrates in winter and summer are 2.4 kg/s and
 502 5.0 kg/s , respectively. In the following, we consider $\Delta \dot{m} \sim (2.4 + 5.0)/2 \sim 4 \text{ kg/s}$ as a rough
 503 estimation of the annual amplitude of the air flowrate. With the mean conduit perimeter $P=9.7$ m
 504 from Table 2 and the air viscosity $\mu_a \approx 1.77 \times 10^{-5} \text{ Pa} \cdot \text{s}$ from Table 1, we get the order of
 505 magnitude of the Reynolds number $Re = \frac{4 \Delta \dot{m}}{P \mu_a} \sim 10^5$. The airflow is thus in the turbulent regime
 506 most of the time. The conduit radius reads $R = P/(2 \pi) \approx 1.5 \text{ m}$ that yields the scaled value
 507 $\tilde{R} = R/L_{dif} \approx 0.3$. The conduit is thus close to the configuration displayed in Figure 4 and
 508 Figure 5 corresponding to $Re = 1.8 \times 10^5$ and $\tilde{R} = 0.189$. In this configuration, cases A and B
 509 yield approximately the same results. The heat transfer is thus limited by conduction in the rock
 510 rather than convection. Therefore, Eq.(24), for which conduction-limited heat transfer is
 511 assumed, is expected to provide a fair estimation of the convection length, and not only a lower

bound. We get $\tilde{L}_0 \approx \tilde{L}_1 \sim 3 \times 10^2$. The theory thus predicts a convection length significantly larger than the conduit length $\tilde{L}_c = L_c/L_{dif} \approx 68$.

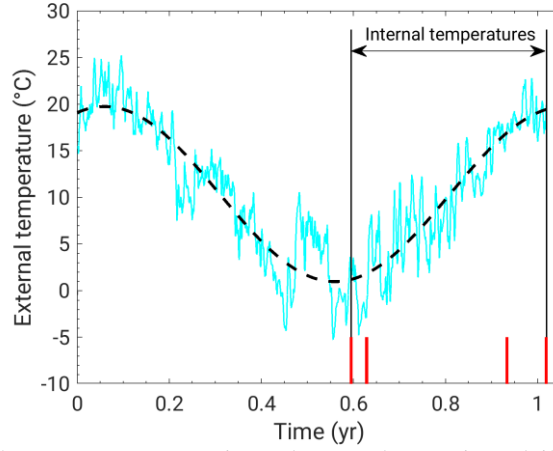


Figure 11: external atmosphere temperature estimated at Baulmes mine (daily averaged data). The horizontal arrow displays the time range during which the temperature inside the cave was measured by the sensors listed in Table 3. The vertical red bars correspond to the dates of the air flowrate measurements listed in Table 4. The black dashed line displays the mode $k=0$ and $k=1$ of the external temperature.

Table 4: air mass flow rate measured in winter and summer.

	Winter (upward flow)		Summer (downward flow)	
Date	02/02/2023	02/15/2023	06/06/2023	7/7/2023
$\tilde{t} = t/\tau_y$	0.595	0.628	0.933	1.018
\dot{m} (kg/s)	1.9	2.8	4.5	5.4

The time series of the external atmosphere temperature and the temperatures inside the conduit have been plotted in Figure 12-left. The dimensionless temperatures inside the conduit are always negative (i.e., lower than the external AMT), even in summer. This is the cold thermal anomaly expected at a lower entrance.

In the following, we assume that the temperature profiles $\theta_w(\tilde{x})$ at time $\tilde{t} = 0.611$ and $\theta_s(\tilde{x})$ at time $\tilde{t} = 1.016$ give an assessment of the coldest and hottest temperatures reached inside the conduit in winter and summer, respectively. These two time-periods are displayed by vertical bars in Figure 12-left, and the corresponding profiles are plotted in Figure 12-right (the temperature at $\tilde{x} = 0$ is the external atmosphere temperature). In winter, the dimensionless temperature continuously increases from -1.6 at the inlet ($\tilde{x} = 0$) to -0.56 at the end of the conduit ($\tilde{x} = 68$). Spatial temperature variations are thus significant over the entire length of the conduit. This suggests that the convection length should be larger than the conduit length. In summer, the reverse flow direction yields a different temperature profile. The temperature at the end of the conduit ($\tilde{x} = 68$) is -0.06, close to the external AMT. When getting closer to the entrance, the temperature decreases to -0.16 at the first probe ($\tilde{x} = 1.9$). The temperature then suddenly increases within the diffusive region, from -0.16 at the first probe ($\tilde{x} = 1.9$) to the positive value 0.78 at the entrance ($\tilde{x} = 0$).

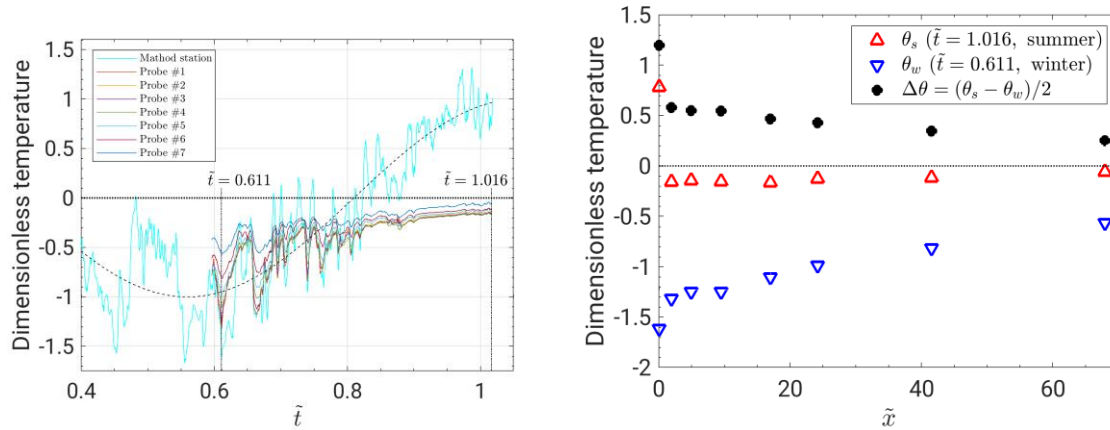


Figure 12: temperatures in Baulmes conduit. Left: daily averaged temperatures as a function of time (the temperature at $\tilde{x} = 0$ is the external atmosphere temperature measured at Mathod weather station). Right: temperature profiles $\theta_s(\tilde{x})$ and $\theta_w(\tilde{x})$ measured respectively in summer and winter, and amplitude of the annual variation $\Delta\theta = (\theta_s - \theta_w)/2$.

The difference $\Delta\theta = (\theta_s - \theta_w)/2$ between summer and winter profiles yields an assessment of the amplitude of the ATF in the conduit. $\Delta\theta$ drops from 1.2 to 0.58 between the entrance ($\tilde{x} = 0$) and the first probe ($\tilde{x} = 1.9$). This sudden decrease takes place in the diffusive region. $\Delta\theta$ then smoothly decreases from 0.58 (first probe at $\tilde{x} = 1.9$) to 0.25 at the end of the conduit ($\tilde{x} = 68$). Assuming that the first sensor yields the temperature at the beginning of the convective region, the amplitude of the temperature fluctuation is thus divided by approximately 2.3 in the convective domain of the conduit. This confirms that the conduit length is significantly shorter than the convection length, defined as the distance required to divide by 10 the ATF measured at the beginning of the convective region (see section 4).

6.2 D7.1 Cave (Sieben Hengste, Switzerland)

D7.1 cave is located in the Sieben Hengste karst area (46°45'5.76"N, 7°48'34.1994"E, 1750 m a.s.l.). It is part of a large ventilated cave system (>160 km of cumulated length) subject to chimney effect. Field observations reveal a seasonal airflow consistent most of the time with an upper entrance of the cave system (i.e., air inflow during the summer season). The ingress of warm external air during summer is marked by some condensation within the first 20 m of the meander, drained as a streamlet at the base of the meander. Otherwise, the cave passage remains remarkably dry. Unexpectedly, temperature and flow rate measurements show periods of time in winter during which the cave sporadically behaves as a lower entrance, with cold air inflow. The explanation of these unexpected flow reversals is still being searched.

External air temperatures displayed in Figure 13-left are provided by an automatic weather station located at 1850 m elevation (SLF), approximately 2 km SE of our study site (sampling period: 1 hour). The external atmosphere temperature was corrected from the elevation as in section 6.1. The FFT yielded $T_m = 5.0^\circ\text{C}$ (after correction) and $\Delta T_y = 7.1^\circ\text{C}$ for the external AMT and ATF, respectively.

The ca. 100 m-long entrance meander of D7.1 Cave has a simple geometry with an average hydraulic diameter of ca. 1 m, despite local variations in the cross-section area and perimeter.

The perimeter $P \approx 3$ m and the scaled radius $\tilde{R} \approx 0.1$ will be considered in the calculations. The meander was instrumented for temperature and airflow measurements between 25/08/2021 and 10/08/2022. Five temperature probes were installed along the main conduit at distances from the cave entrance listed in Table 5. Probes #1 to #4 are Reefnests Sensus Ultra with ± 0.3 °C accuracy (sampling period: 30 min). Probe #5 is a HOBO U22-001 with ± 0.2 °C accuracy (sampling period: 2 hours). It is located at the base of a 20 m shaft following the entrance meander. Time series from the five probes are displayed in Figure 13-right.

Table 5: location of the five temperature probes inside the instrumented conduit of D Cave. x is the distance from the entrance.

Probe	#1	#2	#3	#4	#5
x (m)	2	11	33	93	125
$\tilde{x} = x/L_{\text{dif}}$	0.38	2.1	6.2	18	24

The cave airflow was measured using a low pressure drop flowmeter (Sensirion SFM 3000 with accuracy of 5% and 20% when velocity is higher and lower than 0.3 m/s, respectively; 50 m from cave entrance) and validated with independent flow measurements (CO₂ gauging) on 10/08/2022. The FFT of the air flow yields the order of magnitude $\Delta \dot{m} \sim 0.1$ kg/s rate (red dashed line in Figure 13-left), which results in $Re \sim 7 \times 10^3$. The cave is thus most of the time in the transition between laminar and turbulent regimes. Eq.(24) yields the theoretical convection length $\tilde{L}_0 \approx \tilde{L}_1 \sim 10$. It is important to note that this value must be considered as a lower bound of the convection length. Indeed, Eq.(24) stands for case B (infinite Biot number). At $Re \sim 7 \times 10^3$, case A (finite Biot number) yields a convection length significantly larger than case B (see Figure 8).

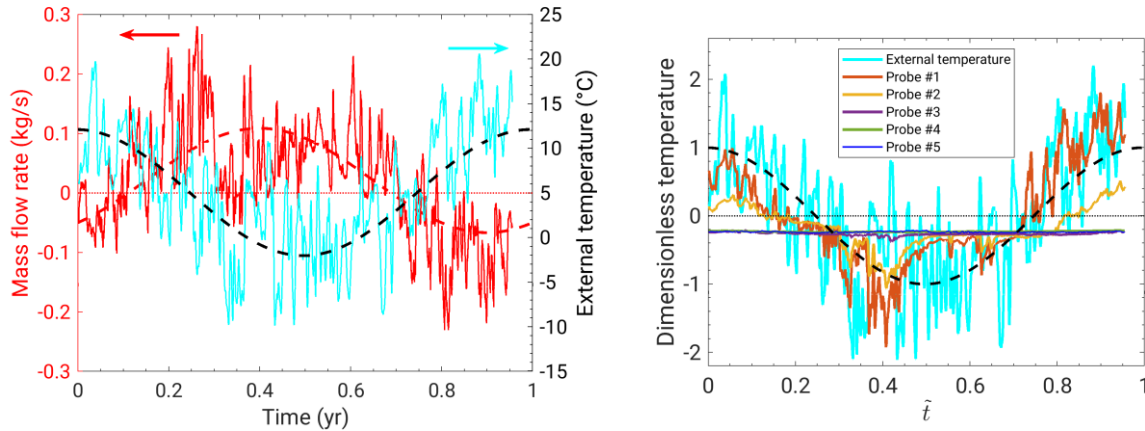


Figure 13 : field data from D7.1 cave. Left: external temperature and mass flow rate; black and red dashed lines represent the modes $k=0$ and $k=1$ computed from the FFT of the external atmosphere temperature and the air flow rate, respectively. Right: external temperature and temperatures inside the cave. All the data are daily averaged.

The AMT inside D7.1 Cave is displayed in Figure 15-left. It decreases to reach a negative quasi-plateau in the range from -0.26 to -0.23 in between probes #3 ($\tilde{x} = 6.2$), and #5 ($\tilde{x} = 24$). This is not the behavior expected for an upper entrance, for which the AMT is supposed to be positive in the convective region before decreasing to zero at some distance from the entrance. Sporadic flow reversals in winter can contribute to this negative AMT (an instance of such an event can be

observed around time $\tilde{t} \approx 0.33$ in Figure 13-left and right). Moreover, the cave entrance is in a topographic low, resulting in local cold air trapping during winter. In addition, snow is likely to accumulate near the cave entrance. Both may induce local free convection cells in the entrance zone in winter resulting in the cooling of the cave below the external AMT.

If we assess \tilde{L}_0 from the distance over which the AMT significantly varies inside the cave, it would range between $\tilde{x} = 2.1$ (probe #2) and $\tilde{x} = 6.2$ (probe #3). This estimation is confirmed by the variation of the ATF with the distance from the entrance (Figure 15-right). The ATF at probe #1 ($\tilde{x} = 0.38$), located in the diffusive region, is close to 1. Then it decreases to 0.36 at probe #2 ($\tilde{x} = 2.1$), the first probe in the convective region, and drops down to 0.02 at probe #3 ($\tilde{x} = 6.2$). The ATF being reduced by a factor larger than 10 between probes #2 and #3, \tilde{L}_1 should be in between these two probes. It is worthwhile to note that this estimation is consistent with the limit of condensation, which falls in between probes #2 and #3 (20 m corresponds to $\tilde{x} \approx 4$). The convection length of D7.1 Cave is thus in the range from 2.1 to 6.2.

6.3 Bärenhöhle Cave (Austria)

The cave is located in Vorarlberg, Austria (47°22'17"N, 9°52'52"E, 901 m asl.). The external atmosphere temperature is obtained from the weather station located at Saint Gallen (47°25'31.7094"N, 9°23'54.7008"E, 776 m a.s.l.), Switzerland about 37 km WNW of our study site (the closer Schopernau station (47°19' N, 10°1'E, 835 m a.s.l.; ZAMG 2012) is subject to thermal inversions during the winter season and thus considered as being less representative). The temperature measured at Saint Gallen has been corrected from the elevation as in section 6.1. It is displayed in Figure 14-left. The FFT yielded $T_m = 8.7^\circ\text{C}$ (after correction) and $\Delta T_y = 7.6^\circ\text{C}$ for the external AMT and ATF, respectively. Chimney effect drives the airflow in the cave which behaves as a lower entrance (air inflow in winter). The difference in elevation between the lower and upper entrances is *ca.* 130 m for a conduit length along the main air passage approximating 240 m (Perkmann and Luetscher, 2013). The average hydraulic diameter is assessed to about 1 m, so that $P \approx 3$ m and $\tilde{R} \approx 0.1$. Air temperature was recorded at 1h interval using three HOBO (U22-001) temperature probes at distances from the entrance listed in Table 6. The corresponding time series are displayed in Figure 14-right.

Table 6: location of the three temperature probes inside Bärenhöhle. x is the distance from the lower entrance.

Probe	#1	#2	#3
x (m)	5	85	120
$\tilde{x} = x/L_{\text{dif}}$	0.95	16	23

Air flow was recorded between 16/04/2013 and 16/04/2014 at the lower entrance using a thermo-anemometer calibrated to ± 0.1 m/s. The FFT of the air flow rate (red dashed line in Figure 14-left) yields the orders of magnitude $\Delta \dot{m} \sim 0.6$ kg/s and $Re \sim 5 \times 10^4$. The cave is thus in the turbulent regime most of the time. In this configuration ($\tilde{R} \approx 0.1$ and $Re \sim 5 \times 10^4$), cases A and B predict approximately the same theoretical convection length (see Figure 8). Eq.(24) yields $\tilde{L}_0 \approx \tilde{L}_1 \sim 70$.

The AMT of Bärenhöhle Cave is displayed in Figure 15-left. Negative values are consistent with a lower entrance. The lowest AMT (-0.27) is measured at probe #2 ($\tilde{x} = 16$). It increases slightly between probe #2 and the last probe #3. The ATF displayed in Figure 15-right decreases over the

whole instrumented conduit, from 1 outside the cave to 0.11 at the last probe ($\tilde{x} = 23$). These two pieces of information suggest that the convection length should be longer than 23, the cave length.

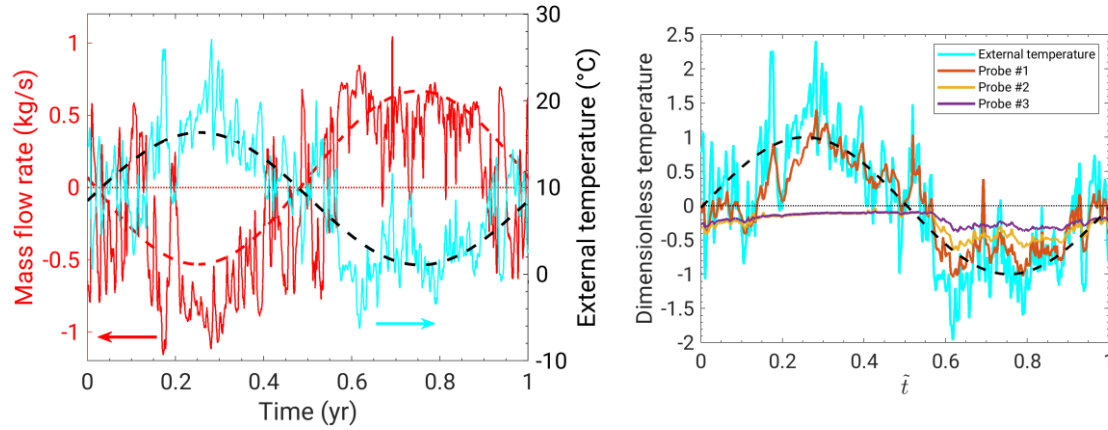


Figure 14: field data of Bärenhöhle Cave. Left: external temperature and mass flow rate; black and red dashed lines represent the modes $k=0$ and $k=1$ computed from the FFT of the external atmosphere temperature and the air flow rate, respectively. Right: external temperature and temperatures inside the cave. All the data are daily averaged.

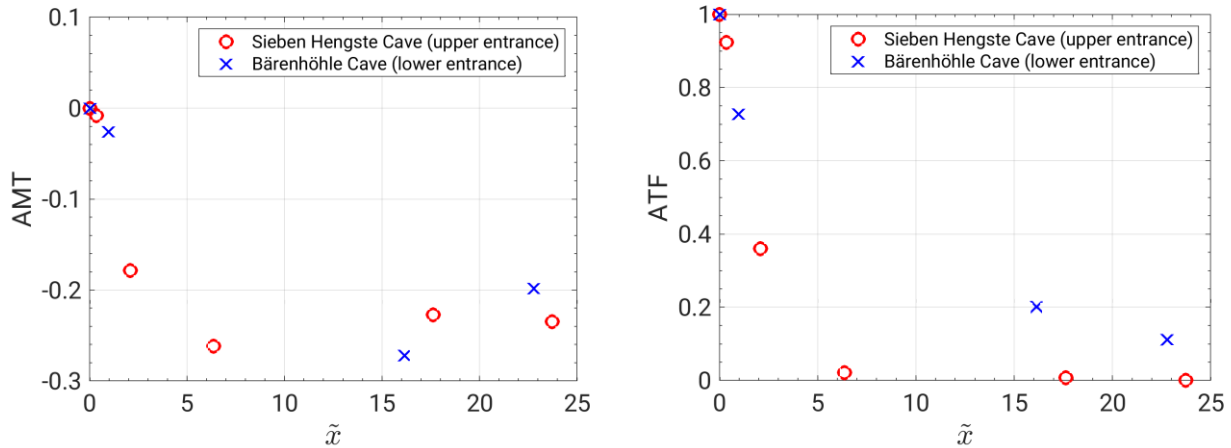


Figure 15: AMT (left) and ATF (right) in Sieben Hengste and Bärenhöhle Caves.

7 Discussion

The main results from the three investigated sites are summarized in Table 7. For two sites (Baulmes mine and Bärenhöhle Cave), we do not observe any contradiction between the model and the field data since both yield a convection length larger than the instrumented conduit (a hundred meters for Bärenhöhle, a few hundreds of meters for Baulmes). In D7.1 Cave, the field data suggest a shorter convection length, in the range from 10 m to 30 m, whereas the theoretical

prediction yields a lower bound of 50 m. Although the theoretical order of magnitude is correct, the theory overestimates the convection length. In a cave with a small Reynolds number and a short convection length, local effects in the entrance region, not considered in the model, could overcome the effect of the mean flow generated by the chimney effect. In the case of D7.1 Cave, cold air ingress in winter might cool down the cave passage more than considered in the model, thus producing an actual shorter thermal length.

Table 7 : Summary table of the three investigated sites (R: cave radius in meters, \tilde{R} : dimensionless cave radius; $\Delta\dot{m}$: amplitude of the air flow rate in kg/s; Re: Reynolds number; \tilde{L}_0 and \tilde{L}_1 : dimensionless convection lengths deduced from the AMT and the ATF, respectively; L_0 and L_1 : same variables in meters.

		Baulmes mine	Sieben Hengste Cave	Bärenhöhle Cave
R		1.5 m	0.5 m	0.5 m
\tilde{R}		0.3	0.1	0.1
$\Delta\dot{m}$		4 kg/s	0.1 kg/s	0.6 kg/s
Re		10^5	7×10^3	5×10^4
$\tilde{L}_0 \approx \tilde{L}_1$	Field data	>68	[2.1 , 6.2]	> 23
	Theory	$\sim 3 \times 10^2$	> 10	~ 70
$L_0 \approx L_1$	Field data	> 360 m	[10 m , 30 m]	> 120 m
	Theory	$\sim 2 \times 10^3$ m	> 50 m	$\sim 4 \times 10^2$ m

Using a theoretical approach, we defined the characteristic lengths \tilde{L}_0 and \tilde{L}_1 from the damping in the convective region of the AMT (mode $k=0$) and ATF (mode $k=1$), respectively. \tilde{L}_0 and \tilde{L}_1 are close to each other, and same values are obtained regardless the wall or the air temperature is considered (see Figure 8). A single convection length is thus sufficient to characterize the extent of the AMT and the ATF along the cave axis. The case B (infinite Biot number) provides a lower bound of the convection length through the simple expression (24). If the Reynolds number is large enough (typically, if $Re > 3 \times 10^4$ for a conduit with a radius of 1 m, see Figure 8), the approximation of infinite Biot number is valid and Eq. (24) is expected to give a right estimation of the convection length. Turning this relation into unscaled variables yields

$$L_0 \approx L_1 \approx 4.0 \times 10^2 \frac{\Delta\dot{m}^{1.06}}{R^{0.45}} \quad (25)$$

where L_0 , L_1 and R are in meters and $\Delta\dot{m}$ in kg/s. Eq.(25) reveals that the convection length is approximately proportional to the amplitude of the flowrate annual fluctuations $\Delta\dot{m}$ divided by the square root of the cave radius R . Ventilated conduits with R of the order of 1 m traversed by an airflow with $\Delta\dot{m}$ ranging from 0.1 kg/s to 1 kg/s are commonly encountered in mines and caves (see the case studies of section 6). For such conduits, Eq.(25) yields a convection length along the conduit axis between a few tens and a few hundreds of meters. Thermal perturbations also propagate in the radial direction, i.e., along the directions perpendicular to the conduit. As expected, the amplitude of the annual fluctuations vanishes over the diffusion length, i.e., a few meters. Conversely, the thermal anomaly (defined as the shift of the annual mean temperature), propagates along distances of the order of $L_0/10$ (see Figure 9), i.e., over distances of the order of a few meters to a few tens of meters. It is worthwhile to note that in some cases, the extent of the thermal perturbation might be much larger than mentioned above. Luetscher and Jeannin (2004) measured air flow rates around 10 kg/s in Hölloch Cave (Switzerland) and La Diau (France).

Recently, airflow rates around 40 kg/s were measured in Shpella Shtares Cave, in Albania (42.31766° N, 19.85403° E, 1427 m a.s.l, see Ref. (Pastore et al., 2019) for more details about this cave). Taking a couple of meters as a rough estimation of the conduit radius in Shpella Shtares, the thermal perturbation should extend over kilometers and hundreds of meters in the axial and radial directions, respectively.

Assessing the thermal penetration length at different time-scales is fundamental to quantify biogeochemical processes in karst systems. Our study demonstrates that seasonal temperature fluctuations propagate from a few tens of meters up to several thousands of meters into a karst system, depending on ventilation rate and conduit geometry. By way of illustration, let us cite the large ice caves in Austria which host perennial ice formations over several hundreds of meters in the lower entrance zone of ventilated cave systems (e.g. Eisriesenwelt; (Obleitner and Spötl, 2011)). However, it is the advent of speleothems as precisely and accurately dated paleoclimate archives which rises the significance of our study. Stalagmites and flowstones are commonly used to reconstruct climate fluctuations based on their isotope (oxygen and carbon) and trace element concentrations (Fairchild and Baker, 2012). In both cases, the proxy partitioning depends strongly on the cave temperature. While it is commonly assumed that the cave temperature at depth is constant, this is only true beyond the convection length which strongly depends on the time-scale of interest.

Because the temperature-dependent oxygen isotope fractionation between water and calcite ranges between -0.18 and -0.21 ‰/°C (Kim and O'Neil, 1997)(Tremaine et al., 2011), seasonal temperature changes >0.5°C represent a significant source of uncertainty in the speleothem-proxy interpretation and it might be of interest to sample beyond the convective region.

Meanwhile, it can be strategic to focus speleothem research on the convective region associated with decadal to millennial cycles, as this area will respond sensitively to outside climate changes without picking up short-term temperature fluctuations.

8 Conclusion

We developed a model coupling buoyancy-induced convection (chimney effect) in a single karst conduit with conduction in the rock mass. We used this model to investigate the propagation of thermal perturbations inside a karst massif. Assuming dry air and a simplified geometry, and reducing the time variations of the external temperature to the annual fluctuations, we performed a parametric study to identify general trends regarding the effect of the air flowrate and conduit size on the amplitude and relaxation length of the thermal perturbations induced by the air flow. The thermal anomaly (defined as a shift in the annual mean temperature) and the annual temperature fluctuations both propagate over the same distances from the entrance. We call this distance the convection length and we show that at high Reynolds number, it is approximately proportional to the air flow rate divided by the square root of the cave radius. The order of magnitude of the theoretical convection length seem to compare satisfactorily with field data obtained from a mine and two caves. Convection lengths of a few tens to a few hundreds of meters should be commonly encountered in ventilated caves. In extreme cases, it could go up to kilometers.

More detailed comparisons between field data and a more elaborated model are currently under investigation. In this first approach, some effects have been neglected on purpose and the significance of condensation/evaporation, daily fluctuations, varying diameter will be further assessed. Moreover, many phenomena are still to be investigated and quantified. We can cite free

convection cells near cave entrances, barometric effects, multiple entrances, water inrush, among others. Our results nonetheless provide first estimates to identify climate sensitive regions for speleothem science and/or ecosystemic studies.

Acknowledgements

This research was funded in whole or in part by the Swiss National Science Foundation (SNSF) [200021_188636]. The data from Bärenhöhle were acquired in the frame of an APART-fellowship from the Austrian Academy of Science granted to ML.

Data Availability Statement

All the model output files for numerical simulations (Comsol files) are available upon request from the authors and all the field data (including the three instrumented sites) can be found in <https://doi.org/10.5281/zenodo.10514555> associated to Sedaghatkish et al (2024).

References

- Atkinson, T. C.: Carbon dioxide in the atmosphere of the unsaturated zone: an important control of groundwater hardness in limestones, *J. Hydrol.*, 35, 111–123, 1977.
- Banner, J. L., Guilfoyle, A., James, E. W., Stern, L. A., and Musgrove, M.: Seasonal variations in modern speleothem calcite growth in central Texas, USA, *J. Sediment. Res.*, 77, 615–622, 2007.
- Bergman, T. L., Lavine, A. S., Incropera, F. P., and DeWitt, D. P.: *Fundamentals of Heat and Mass Transfer*, Wiley, 2017.
- Borsato, A., Johnston, V. E., Frisia, S., Miorandi, R., and Corradini, F.: Temperature and altitudinal influence on karst dripwater chemistry: Implications for regional-scale palaeoclimate reconstructions from speleothems, *Geochim. Cosmochim. Acta*, 177, 275–297, 2016.
- Bourges, F., Genthon, P., Genty, D., Lorblanchet, M., Mauduit, E., and d’Hulst, D.: Conservation of prehistoric caves and stability of their inner climate: lessons from Chauvet and other French caves, *Sci. Total Environ.*, 493, 79–91, 2014.
- Bourret, F., Jeannin, P.-Y., Lalou, J.-C., Lambelet, J., Pauli, C., Spring, D., and Thévoz, P.-Y.: *Inventaire spéléologique de la suisse, Tome v, Nord vaudois*, La Commission de Spéléologie de l’Académie suisse des sciences naturelles, 2007.
- Casteel, R. C. and Banner, J. L.: Temperature-driven seasonal calcite growth and drip water trace element variations in a well-ventilated Texas cave: Implications for speleothem paleoclimate studies, *Chem. Geol.*, 392, 43–58, 2015.
- Covington, M. D., Luhmann, A. J., Gabrovšek, F., Saar, M. O., and Wicks, C. M.: Mechanisms of heat exchange between water and rock in karst conduits, *Water Resour. Res.*, 47, 2011.
- Cropley, J. B.: Influence of surface conditions on temperatures in large cave systems, *Bull. Natl. Speleol. Soc.*, 27, 1–10, 1965.
- Domínguez-Villar, D., Krklec, K., and Sierro, F. J.: Thermal conduction in karst terrains dominating cave atmosphere temperatures: Quantification of thermal diffusivity, *Int. J. Therm. Sci.*, 189, 108282, 2023.

- Domínguez-Villar, D., Krklec, K., López-Sáez, J. A., and Sierro, F. J.: Thermal impact of Heinrich stadials in cave temperature and speleothem oxygen isotope records, *Quat. Res.*, 1–14, n.d.
- Dreybrodt, W., Gabrovšek, F., and Perne, M.: Condensation corrosion: a theoretical approach, *Acta carsologica*, 34, 2005.
- Fairchild, I. J. and Baker, A.: *Speleothem science: from process to past environments*, John Wiley & Sons, 2012.
- Gabrovšek, F.: How do caves breathe: The airflow patterns in karst underground, *PLoS One*, 18, e0283767, 2023.
- Gomell, A., Austin, D., Ohms, M., and Pflitsch, A.: Air pressure propagation through Wind Cave and Jewel Cave: How do pressure waves travel through barometric caves?, *Int. J. Speleol.*, 50, 263–273, <https://doi.org/10.5038/1827-806x.50.3.2393>, 2021.
- Gong, X., Yang, X., Luo, Q., and Tang, L.: Effects of convective heat transport in modelling the early evolution of conduits in limestone aquifers, *Geothermics*, 77, 383–394, 2019.
- Guerrier, B., Doumenc, F., Roux, A., Mergui, S., and Jeannin, P.-Y.: Climatology in shallow caves with negligible ventilation: Heat and mass transfer, *Int. J. Therm. Sci.*, 146, 106066, 2019.
- Haaland, S. E.: Simple and explicit formulas for the friction factor in turbulent pipe flow, 1983.
- Kim, S.-T. and O’Neil, J. R.: Equilibrium and nonequilibrium oxygen isotope effects in synthetic carbonates, *Geochim. Cosmochim. Acta*, 61, 3461–3475, 1997.
- Kukuljan, L., Gabrovšek, F., and Covington, M.: The relative importance of wind-driven and chimney effect cave ventilation: Observations in Postojna Cave (Slovenia), *Int. J. Speleol.*, 50, 275–288, <https://doi.org/10.5038/1827-806x.50.3.2392>, 2021.
- Lismonde, B.: *Climatologie du monde souterrain; Tome 2-Aérologie des systèmes karstiques*, Persée-Portail des revues scientifiques en SHS, 2002.
- Long, A. J. and Gilcrease, P. C.: A one-dimensional heat-transport model for conduit flow in karst aquifers, *J. Hydrol.*, 378, 230–239, 2009.
- Luetscher, M. and Jeannin, P.: Temperature distribution in karst systems: the role of air and water fluxes, *Terra Nov.*, 16, 344–350, 2004.
- Luetscher, M., Lismonde, B., and Jeannin, P.: Heat exchanges in the heterothermic zone of a karst system: Monlesi cave, Swiss Jura Mountains, *J. Geophys. Res. Earth Surf.*, 113, 2008.
- Mammola, S., Piano, E., Cardoso, P., Vernon, P., Domínguez-Villar, D., Culver, D. C., Pipan, T., and Isaia, M.: Climate change going deep: the effects of global climatic alterations on cave ecosystems, *Anthr. Rev.*, 6, 98–116, 2019.
- Obleitner, F. and Spötl, C.: The mass and energy balance of ice within the Eisriesenwelt cave, Austria, *Cryosph.*, 5, 245–257, 2011.
- Pastore, C., Pastore, M., Marraffa, M., Marraffa, A., Romano, R., Crespo, S., Fabbri, I., and Santagata, T.: Albania – Tra le (R)ughe albanesi. Racconti di esplorazioni condivise, *Speleologia*, 80, 38–45, 2019.
- Perkmann, L. and Luetscher, M.: Vermessung und hydrogeologische Untersuchung des Bärenhöhlensystems, Bregenzerwald, Vorarlberg, 64, 32–44, 2013.
- Pethkool, S., Eiamsa-Ard, S., Kwankaomeng, S., and Promvonge, P.: Turbulent heat transfer enhancement in a heat exchanger using helically corrugated tube, *Int. Commun. Heat Mass Transf.*, 38, 340–347, 2011.
- Promthaisong, P., Jedsadaratanachai, W., and Eiamsa-Ard, S.: 3D Numerical study on the flow topology and heat transfer characteristics of turbulent forced convection in spirally corrugated tube, *Numer. Heat Transf. Part A Appl.*, 69, 607–629, 2016.

- 812 Qaddah, B., Soucasse, L., Doumenc, F., Mergui, S., Rivière, P., and Soufiani, A.: Influence of
813 turbulent natural convection on heat transfer in shallow caves, *Int. J. Therm. Sci.*, 177, 107524,
814 2022.
- 815 Qaddah, B., Soucasse, L., Doumenc, F., Mergui, S., and Rivière, P.: Coupled heat and mass
816 transfer in shallow caves: interaction between turbulent convection, gas radiative transfer and
817 moisture transport, *Int. J. Therm. Sci.*, 2023.
- 818 Quindós, L. S., Bonet, A., Díaz-Caneja, N., Fernández, P. L., Gutiérrez, I., Solana, J. R., Soto, J.,
819 and Villar, E.: Study of the environmental variables affecting the natural preservation of the
820 Altamira Cave paintings located at Santillana del Mar, Spain, *Atmos. Environ.*, 21, 551–560,
821 1987.
- 822 Salmon, F., Lacanette, D., Lharti, H., and Sirieix, C.: Heat transfer in rock masses: Application
823 to the Lascaux Cave (France), *Int. J. Heat Mass Transf.*, 207, 124029, 2023.
- 824 Sedaghatkish, A., Pastore, C., Doumenc, F., Jeannin, P.-Y., and Luetscher, M.: field data for
825 Modelling heat transfer for assessing the convection length in ventilated caves, 2024.
- 826 Sinokrot, B. A. and Stefan, H. G.: Stream temperature dynamics: measurements and modeling,
827 *Water Resour. Res.*, 29, 2299–2312, 1993.
- 828 Spötl, C., Fairchild, I. J., and Tooth, A. F.: Cave air control on dripwater geochemistry, Obir
829 Caves (Austria): Implications for speleothem deposition in dynamically ventilated caves,
830 *Geochim. Cosmochim. Acta*, 69, 2451–2468, 2005.
- 831 Tremaine, D. M., Froelich, P. N., and Wang, Y.: Speleothem calcite farmed in situ: Modern
832 calibration of $\delta^{18}\text{O}$ and $\delta^{13}\text{C}$ paleoclimate proxies in a continuously-monitored natural cave
833 system, *Geochim. Cosmochim. Acta*, 75, 4929–4950, 2011.
- 834 Villar, E., Fernández, P. L., Quindós, L. S., Solana, J. R., and Soto, J.: Temperature of rock
835 surfaces in Altamira Cave (Spain), *Trans. Br. Cave Res. Assoc.*, 10, 165–170, 1983.
- 836 Wigley, T. M. L. and Brown, C.: Geophysical applications of heat and mass transfer in turbulent
837 pipe flow, *Boundary-layer Meteorol.*, 1, 300–320, 1971.
- 838